



This article appeared in a journal published by Elsevier. The attached copy is furnished to the author for internal non-commercial research and education use, including for instruction at the authors institution and sharing with colleagues.

Other uses, including reproduction and distribution, or selling or licensing copies, or posting to personal, institutional or third party websites are prohibited.

In most cases authors are permitted to post their version of the article (e.g. in Word or Tex form) to their personal website or institutional repository. Authors requiring further information regarding Elsevier's archiving and manuscript policies are encouraged to visit:

<http://www.elsevier.com/copyright>



Contents lists available at ScienceDirect

## Computers and Chemical Engineering

journal homepage: [www.elsevier.com/locate/compchemeng](http://www.elsevier.com/locate/compchemeng)

## Image based meshing of packed beds of cylinders at low aspect ratios using 3d MRI coupled with computational fluid dynamics

M.J. Baker, P.G. Young, G.R. Tabor\*

College of Engineering, Mathematics and Physical Sciences (CEMPS), Harrison Building, University of Exeter, North Park Road, Exeter EX4 4QF, UK

## ARTICLE INFO

## Article history:

Received 30 November 2009

Received in revised form 10 March 2011

Accepted 12 March 2011

Available online 22 March 2011

## Keywords:

Packed bed

Pressure drop

MRI

CFD

## ABSTRACT

CFD is a valuable tool for understanding the flow and pressure drop in packed beds. However, determining the geometry can be complex. One possible method is to use a non-invasive imaging method such as MRI, however, problems occur in processing complex geometries when using traditional commercial meshing software. This work focuses on the use of image based meshing software originally developed for the field of computational biomechanics, to create geometries from 3d MRI scans of packed beds for use with computational dynamics. For this work we focus on disordered packed beds of cylinders at low aspect ratios and Reynolds numbers of  $Re = 1431$ – $5074$  (based on particle diameter and superficial velocity). We compare CFD studies with experimental data performed on the actual scanned beds and compare these with the correlation proposed by [Eisfeld and Schnitzlein \(2001\)](#). Computational data is shown to correlate well with experimental and theoretical results.

© 2011 Elsevier Ltd. All rights reserved.

## 1. Introduction

A packed bed is essentially a number of macroscopic particles packed into a particular volume and thus unable to move. This creates a network of connecting spaces through the bed through which fluid can flow. The particles can be random in size or shape, such as charcoal or gravel, or can be regular, such as uniformly sized spheres. In addition, the packing regime can display a unstructured random fashion, or a structured pack, such as a close hexagonal or face centre cubic packing. The selection of particles is crucial and can significantly affect the packed bed's performance by altering the void volumes between the particles, or by changing the bed surface area. Packed beds are used extensively in industry for absorption, stripping and distillation operations ([Perry & Green, 1997](#)) (e.g. the cracking of hydrocarbons, industrial filtration, and heat storage). As a result of this there has been much interest in the characteristics and behaviour exhibited by packed beds.

When considering the characteristics of a packed bed certain parameters are of interest to researchers and engineers. Primarily, the drop in pressure caused by the media is of most interest, but also the dwell time and fluid to particle interaction are also important. Traditional methods for determining pressure drop involve experiments where the pressure difference is taken immediately before and after the bed or at intervals through the bed, as a fluid percolates through it. Theoretical derivations based on simplified geometric

models have also been investigated. Many correlations exist to calculate the pressure drop, such as those reported by [Blake \(1922\)](#) and [Kozeny \(1927\)](#) for laminar flow and by [Burke and Plummer \(1928\)](#) and [Carman \(1938\)](#) for turbulent flow. Derived from the correlations of [Blake \(1922\)](#), [Kozeny \(1927\)](#), [Burke and Plummer \(1928\)](#), and [Carman \(1938\)](#) is the well established Ergun equation developed in the 1950s ([Ergun, 1952](#)), which predicts pressure drop per-unit length through a packed bed for both turbulent and laminar flow regimes. However the Ergun equation is limited to relatively high aspect ratios, where the aspect ratio is the ratio of the particle diameter to the tube diameter ( $N = D/d_p$ ). [Foumeny, Benyahia, Castro, Moallemi, and Roshani \(1993\)](#) suggest that when the aspect ratio is  $<50$  the Ergun equation yields a poor result. One of the most promising correlations to predict the pressure drop through a packed bed is that proposed by [Reichelt \(1972\)](#). The equation is further modified by the addition of coefficients based around a regression of 2300 experimental data points from 27 published results ([Eisfeld & Schnitzlein, 2001](#)).

Experimental and theoretical approaches give a good indication of pressure drop, but do not allow quantitative analysis of the flow distributions within the bed. CT and 3d MRI imaging techniques have also proved invaluable for analysing these aspects of packed beds ([Montillet & Coq, 2001](#)). [Zhang, Thompson, Reed, and Beenken \(2006\)](#) couple non-invasive methods with a digital packing algorithm. They use the code DigiPac which combines both Monte-Carlo methods and Discrete Element methods and compare this with beds analysed using MRI. They investigate bed voidage distribution and packing density of packed beds of cylinders. [Sharma, Mantle, Gladden, and Winterbottom \(2001\)](#) use magnetic resonance imag-

\* Corresponding author.

E-mail address: [g.r.tabor@ex.ac.uk](mailto:g.r.tabor@ex.ac.uk) (G.R. Tabor).

ing to investigate bed voidage, pressure drop and bed density in packed bed reactors. They conclude that in all cases, analysis of MRI data results in voidage values which are consistently higher than values determined from water substitution. Ren, Stapf, and Blumich (2005) use MRI coupled with velocity encoding and pulsed-field-gradient nuclear magnetic resonance (PFG-NMR) to investigate the flow structure within packed beds of cylinders and spheres with aspect ratios of 1.4–32.

Computational techniques, in particular computational fluid dynamics (CFD) have also been applied to probe the flow through the bed, and these provide the most detailed picture of the microstructure of the flow. Despite constant advances in computing power and development of mathematical methods, it is still not yet possible to perform a 3d simulation of a full-size industrial scale fixed bed reactor (Freund, Bauer, & Zeiser, 2005). A significant problem associated with computational methods is determining the complex bed geometry needed to analyse the bed in detail. The most simplistic way of determining a packed bed geometry is to assume a regular packing and use simple geometric relations, such as face centred cubic for spheres or close hexagonal packing regimes. The flow can then be computed for a single unit cell and extrapolated from that to the entirety of the bed. As an example of this, Gunjal, Ranade, and Chaudhari (2005) employ a single unit-cell approach of an array of spheres encompassing simple cubical, 1d rhombohedral, 3d rhombohedral and face-centre cubic structures, coupled with CFD and investigate interstitial flow in the void space.

A unit-cell approximation makes the calculation reasonably tractable. However for random, unstructured, packed beds the true geometry is complex and tortuous, and a single unit cell may not be considered representative. Instead a larger section of the bed must be simulated, large enough to contain a significant and representative diversity of microstructure and thus hopefully large enough to be considered representative of the microstructural flow. Creating (and subsequently meshing) this geometry is a highly challenging task. One way of achieving this is by creating an artificial bed using a digital packing algorithm (Baker & Tabor, 2010; Chaulkin, Ahmad, Fairweather, Jia, & Williams, 2007, 2009). Another possibility is to use MRI or CT to probe the geometric structure of a real bed and create a computational domain which can be used to simulate the flow, and this is the target of our work reported here. Some attempts have been made to do this before, such as (Manz, Warren, & Gladden, 1999), who use Lattice Boltzmann simulations based on an MRI visualisation of a packed bed for Reynolds numbers  $0.4 < \text{Re} < 0.77$  (i.e. in the creeping flow regime). Mantle, Sederman, and Gladden (2001) use 3d MRI and MRI velocimetry (MRV) to characterise the structure of the interparticle void space and three components of velocity within the voids and compare this with Lattice Boltzmann simulations. In both these cases the volume of interest for computational simulation is determined directly from the 3d MRI data by partitioning the void volume from the particles, and in both cases the Lattice Boltzmann method is used to perform the calculations. The Boltzmann transport equations describe the statistical distribution of particles in a fluid. In the LB method these are represented by a limited number of fictitious particles that represent the statistical properties of groups of molecules in the fluid. Particle velocities are restricted to a finite set of discrete values and directions on a highly structured lattice which has a 1-to-1 correspondance with the voxels of the MRI scan. The resulting method is very fast and efficient, but the structured lattice means that complex boundaries are pixelated. Both papers compare the microstructural flow from the Lattice Boltzmann simulation with detailed measurements from the MRI, but do not compare macroscopic parameters of the bed such as overall pressure drop.

The aim of the work described in this paper is to perform CFD calculations on meshes developed from MRI scans of real packed beds.

Fig. 1 shows a flow chart of the links between the experimental work and the various computational elements being undertaken. In contrast to the earlier work using the Lattice Boltzmann approach described above, our approach uses the finite volume (FV) technique in which the full Navier–Stokes equations are solved on a body-fitted mesh using the commercial CFD package Fluent. We utilise image based meshing (IBM) methods originally devised for biomechanical problems to create the bed geometry and mesh based on an MRI scan of a packed bed of cylinders, again using commercially available codes (ScanIP and ScanFE). Although this work is primarily a computational study, in order to validate the computational data, experiments were carried out on the actual scanned beds. Experimental pressure differences were calculated using pressure tapping before and after the packed bed and at 0.1 m increments through the bed. Air was forced through the bed by means of a centrifugal pump. Volumetric flow rate and hence average velocity across the profile was measured by the differential pressure across a plate orifice positioned before the bed. The range of Reynolds numbers and thus flow conditions examined was much higher, corresponding to transitional and turbulent flow in the bed, and the work focusses on accurate prediction of macroscopic parameters (predominantly the pressure drop). Similar work has been applied to foams in the past (Tabor, Yeo, Young, & Laity, 2008) but as far as we know this is the first application of these techniques to a packed bed.

## 2. Theory of packed beds

Many correlations exist to calculate pressure drop through a packed bed, such as the well established correlations of Blake (1922), Kozeny (1927) and Ergun (1952). These correlations accurately model pressure drop for high aspect ratio cases ( $N = d_p/D$ ), but when the aspect ratio is  $< 50$  the Ergun equation yields a poor result (Foumeny et al., 1993). Choi, Kim, and Kim (2008) suggest that when the diameter of the particle ( $d_p$ ) is not significantly smaller than the tube diameter ( $D$ ) the flow distribution and wall friction are not negligible. In this case many alternative correlations exist to account for the influence of the confining wall (DiFelice & Gibilaro, 2004; Choi et al., 2008; Reichelt, 1972). In this work, we report our experimental and computational results in the form of dimensionless pressure drop,  $\phi$ , defined as

$$\phi = \frac{\Delta P}{\rho_0 U^2} \frac{d_p}{L} \quad (1)$$

where  $U$  is the superficial velocity (the average velocity in the pipe upstream of the bed). In most cases associated with the motion of a fluid it is desirable to determine the Reynolds number and hence characterise the flow as laminar, transitional or turbulent. The Reynolds number is defined as the ratio of the viscous and inertial forces with the inclusion of a scaling function, for pipe flow, usually pipe diameter. For this work we use the particle Reynolds number where the scaling function is the diameter or equivalent diameter of the particle, given as

$$\text{Re}_{dp} = \frac{\rho U d_p}{\mu} \quad (2)$$

where laminar flow occurs for  $\text{Re}_{dp} < 10$ , transitional for  $10 < \text{Re}_{dp} < 300$ , and turbulent flow  $\text{Re}_{dp} > 300$  (Ziolkowska & Ziolkowska, 1988). However, values can vary substantially between different cases. Based on this the flow regimes studied in this work are likely to be transitional progressing to turbulent flow due to the heterogeneous bed geometry. However, in the case of low aspect ratio, disordered beds such as this, all three flow regimes are likely to exist. In the case of non-spherical particles (such as this), the equivalent diameter is used, which is defining the

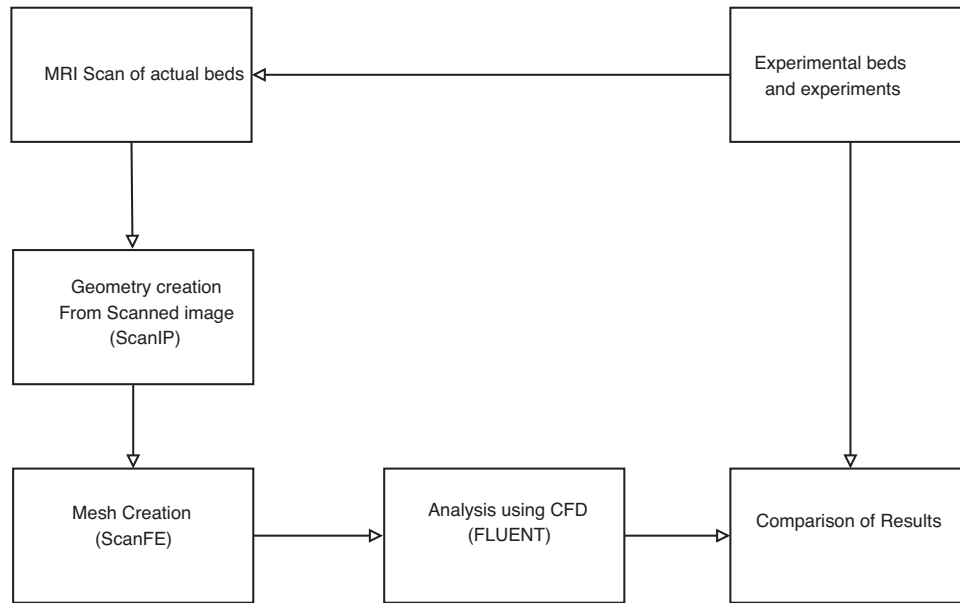


Fig. 1. Flow chart illustrating the links and dependencies between various elements of computational and experimental work described in the paper.

equivalent particle size by the diameter of a sphere of equivalent surface area (Carman, 1937; Eisfeld & Schnitzlein, 2001) given as

$$d_p = \frac{6V_p}{S_A} \quad (3)$$

The equivalent diameter of the cylindrical media used in this work is calculated as 22.5 mm.

Carman (1937) suggests that in laminar flow, the dimensionless pressure drop  $\phi$  is proportional to  $1/\text{Re}_{dp}$ . Here, we compare both experimental and computational with the correlation described by Reichelt (1972) using the fitted coefficients determined by Eisfeld and Schnitzlein (2001) as

$$\phi = \frac{K_1 A_W^2 (1 - \varepsilon)}{\text{Re}_{dp} \varepsilon^3} + \frac{A_W (1 - \varepsilon)}{B_W \varepsilon^3} \quad (4)$$

Values of  $K_1$  for cylindrical media are given as  $K_1 = 154$  and  $k_1 = 190$  (Eisfeld & Schnitzlein, 2001).

$$A_W = 1 + \frac{2}{3(D/d_p)(1 - \varepsilon)} \quad (5)$$

and

$$B_W = \left[ k_1 \left( \frac{d_p}{D} \right)^2 + k_2 \right]^2 \quad (6)$$

### 3. Computational fluid dynamics

Computational fluid dynamics is the use of computers to solve problems associated with the motion of a fluid. Traditionally it is usually taken to mean the solution of the governing equations, the Navier–Stokes equations in 2 or 3 dimensions for laminar or streamline flow, or the averaged Navier–Stokes equations together with a turbulence model in the case of a turbulent flow. As described above the range of Reynolds numbers being investigated ranges from laminar through transitional to mildly turbulent, but the structure of the bed is likely to encourage the development of disordered, stochastic flow (if not true turbulence) even for strictly laminar conditions. Conversely the requirement to resolve the structure of the bed indicates the necessity to resolve the flow with a fine mesh, so one of the main contributions of a turbulence model,

that of substituting for the effect of unresolved scales, is not relevant. Accordingly, calculations were run using both laminar and turbulence modelling, and compared.

For the laminar modelling, the equations being solved are as follows:

$$\nabla \cdot \underline{u} = 0$$

$$\frac{\partial \underline{u}}{\partial t} + \nabla \cdot \underline{u} \underline{u} = -\frac{1}{\rho} \nabla p + \nu \nabla^2 \underline{u} \quad (7)$$

For turbulence modelling, an averaging process is applied to the equations. Most often this is an ensemble or time averaging, known as Reynolds averaging, which generates the Reynolds Averaged Navier–Stokes (RANS) equations:

$$\nabla \cdot \hat{\underline{u}} = 0$$

$$\frac{\partial \hat{\underline{u}}}{\partial t} + \nabla \cdot \hat{\underline{u}} \hat{\underline{u}} + \nabla \cdot \underline{\underline{R}} = -\frac{1}{\rho} \nabla p + \nu \nabla^2 \hat{\underline{u}} \quad (8)$$

where  $\hat{\underline{u}}$  denotes a Reynolds-averaged flow variable, and  $\underline{\underline{R}}$  is an additional term called the Reynolds Stress, which represents the effect of the turbulence (which has been removed by the averaging procedure) on the mean flow. In complex geometries such as flow through packed beds the 3d Navier–Stokes equations have no exact solution, and in fact the nature of the equations does not even guarantee that a single answer will exist (Logtenberg & Dixon, 1998).

Various models are possible to describe the Reynolds Stress term. Most commonly used are models based on the eddy viscosity concept, in which the effect of the turbulence is taken to be equivalent to the enhancement of the viscosity of the fluid, so  $\underline{\underline{R}}$  is modelled as  $\nu_t \nabla^2 \hat{\underline{u}}$ . In turn, the turbulent viscosity  $\nu_t$  is modelled in terms of additional variables for which transport equations are solved. In the commonly used  $k$ – $\varepsilon$  model, the turbulent kinetic energy  $k$  and the turbulent dissipation  $\varepsilon$  are used, in terms of which the eddy viscosity is given by

$$\nu_t = C_\mu \frac{k^2}{\varepsilon}$$

where  $C_\mu$  is a dimensionless coefficient determined by validation against experiment. The exact details of the transport equations for  $k$  and  $\varepsilon$  lead to various variants of the basic model; standard  $k$ – $\varepsilon$ ,



RNGk- $\varepsilon$ , and various low Reynolds number models. An alternative family of models is derived using the turbulence frequency  $\omega = \varepsilon/k$  as an alternative to  $\varepsilon$  in order to set the length scale of turbulence in the flow.  $\omega$  has a number of advantages, one being that  $\omega \rightarrow 0$  at the wall, which is particularly convenient for lower Reynolds number conditions. In the standard  $k$ - $\omega$  model  $k$  and  $\omega$  are obtained from the following set of partial differential equations

$$\frac{\partial}{\partial t}(\rho k) + \nabla \cdot (\rho k \underline{\hat{u}}) = \nabla \cdot (\Gamma_k \nabla k) + G_k - Y - \kappa + S_k \quad (9)$$

and

$$\frac{\partial}{\partial t}(\rho \omega) + \nabla \cdot (\rho \omega \underline{\hat{u}}) = \nabla \cdot (\Gamma_\omega \nabla \omega) + G_\omega - Y - \omega + S_\omega \quad (10)$$

where  $G_k$  is turbulent kinetic energy generation as a result of the average gradients in velocity,  $G_\omega$  is the specific dissipation rate.  $\Gamma_k$  and  $\Gamma_\omega$  are the effective diffusivities.  $S_k$  and  $S_\omega$  are source terms.  $Y_k$  and  $Y_\omega$  represent the turbulent dissipation of  $k$  and  $\omega$ .

The  $k$ - $\omega$  SST model (Menter, 1994) is a blend of the  $k$ - $\omega$  and  $k$ - $\varepsilon$  models, aimed to combine the beneficial aspects of the  $k$ - $\omega$  model near-wall with the better behaviour of the  $k$ - $\varepsilon$  in the free stream (its behaviour is less sensitive to the exact values of the coefficients). The  $k$  equation from the  $k$ - $\omega$  model is used combined with a modified  $\omega$  equation derived from the  $\varepsilon$  equation; this includes the addition of a cross diffusion term added to Eq. (10) where the diffusive term is defined as

$$D_\omega = 2(1 - F_1)\rho\sigma_{\omega,2}\frac{1}{\omega}\nabla k \cdot \nabla \omega \quad (11)$$

The  $k$ - $\omega$  SST model is particularly appropriate for low Reynolds number and transitional flows, and so this turbulence model was adopted for the turbulent simulations.

We solve the governing Eqs. (7) and (8) using the finite volume approach. In this, the domain of interest is divided into numerous small cells, and the governing equations integrated over the volume of each cell. Gauss's theorem is used to convert the spatial derivative term  $\nabla \cdot (\underline{\hat{u}}\underline{\hat{u}})$  into a surface integral of the flux across the faces bounding the cell, which converts the governing equations into a set of difference equations which can be solved numerically. For this we use the commercial CFD code Fluent; interpolation from cell centre to cell face is carried out using the second order upwind differencing for the momentum equation, and the non-linear nature of the equations is treated iteratively, using PISO for transient calculations and SIMPLE for steady state calculations. The SIMPLE algorithm (Semi-Implicit Method for Linked Equations) is an iterative method for solving the equations via a pressure correction equation developed by Patankar and Spalding (1972) (Versteeg & Malalasekera, 1995). The algorithm PISO, which stands for Pressure Implicit with Splitting of Operators (Issa, 1986), involves a single predictor step and two corrector steps (Versteeg & Malalasekera, 1995). Essentially the PISO algorithm is a variant of the SIMPLE algorithm with the inclusion of an extra corrector step for enhancement (Versteeg & Malalasekera, 1995). Trial studies with a variety of solvers (SIMPLE, SIMPLEC, PISO) indicated that in these particular cases the final output ( $\Delta P$ ) was fairly insensitive to the exact algorithm used.

The inlet boundary was a fixed velocity inlet condition as implemented in Fluent; this is spatially uniform over the inlet. Whilst for purely laminar flow in a pipe the radial profile is parabolic, for turbulent flow the fully developed profile in a pipe is much flatter (traditionally taken as a 1/7th profile) and a uniform inlet was thought to be close enough for this purpose. At the outlet a constant pressure boundary condition was used, sufficiently far downstream as to ensure that this has no back-propagation effects on the flow in the bed. To ensure stability, simulations were run initially using the steady state solver and then using this as initial conditions, progressing to an unsteady solver. To ensure computational stability



Fig. 2. Image produced from 3d MRI.

when implementing the  $k$ - $\omega$  model, studies were first run using first order differencing for pressure for 2000 iterations, progressing to the second order discretisation and the second order upwind differencing for momentum. Courant numbers for the unsteady solver were deliberately kept low ( $1 \times 10^{-5}$ ) to ensure stability. Convergence to a solution was judged based on the mass flow rate at the outlet of the domain. Typical run times were of the order of 12 h in parallel on  $4 \times 2.6$  GHz AMD Opteron processors.

#### 4. Experimental data

No CFD method is 100% reliable. There is always a level of uncertainty involving user inputs, numerical error and other factors. Additionally, as it is basically a human-constructed model, only known factors can be included into the calculation; CFD can never be used to investigate unknown factors. Due to such uncertainties CFD data is best reinforced with experimental data, no matter how rudimentary, to give some validity to the solution. To this end, experimental pressure drops were measured using the experimental rig described in Baker and Tabor (2010). The rig is based on that of Tóbiš (2000), with the addition of pressure taps into the bed at 0.1 m vertical intervals. Air was forced through the bed using a centrifugal pump. Volumetric flow rate  $Q$ , and hence average velocity  $U$ , was determined by measuring differential pressure ( $\Delta P$ ), across a plate orifice manufactured from Perspex and previously calibrated. Experimental pressure drop in this work was calculated by means of a differential micro-manometer attached to a data logger. The data logger readings were averaged to reduce error from small fluctuations in pressure due to turbulence. To generate the cylindrical particles for the bed, PVC rods of diameter 20 mm were cut to lengths of 30 mm and packed randomly into a tube of diameter 100 mm, forming an experimental bed of length 300 mm.

The other experimental aspect is the determination of the geometry of the packed bed using MRI. The packed bed was scanned using a Philips 1.5 T whole-body imager using 2d fast spin echo (FSE). Resolution for this is  $(1.0 \text{ mm})^3$ ; the scan generates a series of 2d images with a pixel resolution of  $1.0 \text{ mm} \times 1.0 \text{ mm}$  with a slice spacing of 1.0 mm. To allow the scanner to distinguish between the particles and the volumes between the particles, the void space was filled with distilled water and any air removed using a vacuum chamber. A typical image produced from the scan is shown in Fig. 2. A section

of the bed of length 120 mm was scanned and used for the computational work. The exact length of bed is not directly important as the results are presented in terms of pressure drop per unit length. Image based meshing techniques, as described in the next section, were used to generate the geometry from this and to create a FV mesh for the solution.

One of the most influential parameters concerning the drop in pressure caused by the presence of the media is porosity. Porosity  $\varepsilon$  is defined by the ratio of the volume of voids ( $V_v$ ) and the total volume ( $V$ ), so  $\varepsilon = V_v/V$ , and is related to the packing fraction given as  $p = (1 - \varepsilon)$ . In this case we take the volume of voids as the mesh volume. In cases of high aspect ratios (such as a packed bed of sand) the porosity can be defined as being homogenous with no measurable wall effect. When a bed is defined as being low aspect ratio the porosity is heterogenous and can be broken down into two distinct regions of wall porosity and core porosity. The traditional method of measuring porosity is usually via water substitution, however this only has the ability to determine mean porosity, whereas bulk and core porosity are harder to determine and are usually calculated theoretically by approaches such as that of DiFelice and Gibilaro (2004). Alternatively, non-invasive approaches, such as MRI and CT can be used to investigate void volume and hence local porosity (Nguyen, van Buren, Reimert, & von Garnier, 2005; Wang, Afacan, Nandakumar, & Chuang, 2001; Zhang et al., 2006). As described below, we use image based meshing techniques to generate body-fitted finite volume meshes from our MRI scans of the beds. Given these it is straightforward to calculate the volume of the mesh (i.e. the volume of the fluid region around the particles) and the total bed volume, and assess the porosity in this way. Both experimental and computational approaches are subject to experimental error; in particular, the start and end positions of the beds are not well defined, and this is a significant issue for such a small bed (this would not be an issue for an industrial-sized bed as this would be significantly larger). Computational porosities are compared to the water displacement method to verify results. Sharma et al. (2001) suggest that the analysis of MRI data yields consistently higher values of porosity in comparison to water substitution; however in our case the porosity determined via MRI coupled with image-based method yielded a slightly lower porosity than that from water substitution. For the cylinders the computational porosity was evaluated as  $\varepsilon_{\text{MRI}} = 0.53$  against  $\varepsilon_{\text{EXP}} = 0.54$  for the experimental value.

## 5. Image based meshing

In computational biomechanics, a frequently encountered problem is that of defining, describing and meshing the geometry of interest. Biological geometries such as arteries or bronchial pathways tend to be complicated and difficult to describe, and also patient-specific; however the flow conditions can be very sensitive to the details of the geometry (Collins, Tabor, & Young, 2007). As a result there is a significant interest in techniques for automatically generating geometries and meshes from medical scans such as MRI scans, which inherently provide 3d geometric information. This is known as image based meshing, or IBM. The fundamental problem of generating a mesh for a complex, unknown geometry based on a 3d scan occurs in a number of other areas of engineering (Tabor, Young, Beresford-West, & Benattayallah, 2007) and in particular is the problem we face when trying to construct a geometrically accurate representation of our packed beds.

There are two general approaches to IBM in existence. One is to generate bounding surfaces from the 3d scans, generally by employing some form of edge detection algorithm. The resulting surfaces (generally saved as STL files) can then be used by standard automatic mesh generation software to create the volumetric

mesh. This works for topologically simple geometries, however applied to highly complex and multiply connected domains such as are the case for packed beds, the surface description will be exceedingly complex and meshing is likely to fail. Even when successful, when computational meshes are created using a traditional delaunay-triangulation approach the meshes often contain large quantities of highly skewed elements and non-positive volumes primarily around the areas of particle contact points.

The alternative is to combine the geometric detection and mesh creation stages in a single process, an approach which is used in the software ScanIP/ScanFE (Simpleware Ltd, Exeter, UK) used in this work. The process of generating a mesh involves first segmenting the different volumes of interest (VOI) from the 3d data. Both semi-automated and manual techniques are available within ScanIP, as well as a range of alternative image processing packages, to provide segmented masks. Techniques include noise filters, three dimensional thresholding tools through to bitmap painting. The resulting mask is then passed to a separate program, ScanFE, for meshing. The VOI are simultaneously meshed based on an orthotropic grid intersected by interfaces defining the boundaries. In effect a base Cartesian mesh of the whole volume defined by the sampling rate is tetrahedralised at boundary interfaces based on cutting planes defined by interpolation points. Smooth boundaries are obtained by adjusting the interpolation points in one, or a combination, of two ways: by setting points to reflect partial volumes or by applying a multiple material anti-aliasing scheme. The process results in either a mixed tetrahedral/hexahedral mesh or a pure tetrahedral mesh and incorporates an adaptive meshing scheme. The adaptive meshing scheme preserves the topology but reduces the mesh density where possible towards the interior of the mesh by agglomerating hexahedra into larger hexahedra and generating transitional tetrahedra. The approach is fully automated and robust creating smooth meshes with low element distortions regardless of the complexity of the segmented data. It is also quite rapid; mesh generation from the packed bed scans here typically took 1–2 h human time, including image import and cleanup, segmentation, meshing and export; within this the meshing algorithm itself takes typically a few minutes to run. This software was originally developed for FE analysis of bones, for both stress and vibration analysis (Johnson & Young, 2005; Puyou, Charriere, Streicher, & Young, 2004; Young et al., 2008; Zunarelli & Young, 1999). Since FE and FV meshes are conjugate structures, the same techniques can be used to output a FV mesh (cell/face representation, rather than point/edge representation). From this method, surface models suitable for rapid prototyping can also be generated which are exact representations of the meshed domains. Amongst other things this also allows experimental tests to be carried out to provide experimental corroboration of numerical results.

The quality of the scans is such that the MRI data is virtually binary, with the majority of voxels taking values 0 and 255 and virtually nothing in between. Thus segmenting the data is very straightforward. Although ScanIP provides various filters, such as Gaussian and noise reduction, to reduce noise in the image, the binary characteristic of the data meant that no preprocessing of the image stack was necessary, and the flow domain mask was easily segmented as the inverse of the bed particles (white areas in Fig. 2). The scan is of course not perfect, but represents a pixelation of the true geometry. This is particularly the case where the cylinders touch; two spheres touch at a mathematical point, but this has to be represented by at least a single voxel, and often the scanned elements are seen to merge, which can be seen in Fig. 3. In effect these contact points form the major constraint when constructing a suitable mesh of minimal skewness. Thus, the IBM approach gains its robustness from increasing the size of the contact points in the voxelising process, reducing the need to create overly skewed elements interparticulate contact region. The practical effect of this is

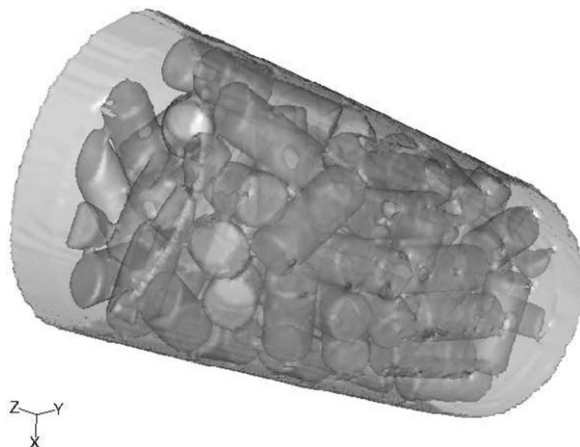


Fig. 3. Packed bed of cylinders recreated using ScanIP and ScanFE.

to increase the volume of space occupied by the bed particles and reduce the porosity, as described above. ScanIP also provides facilities whereby the segmented mask can be dilated or eroded by a pixel or a fraction of a pixel, resulting in smaller or larger bed particles and higher or lower porosity. However the overall porosity was close enough to the experimentally determined value and so this was not thought necessary.

In the FV technique the domain is divided into finite volumes or cells which in standard practice are represented by flat-sided polygons (tetrahedral, hexahedral, etc.). This makes meshing rounded and spherical surfaces technically impossible without an infinitely fine mesh or the use of higher order cells with curved faces (such as NURBS patches). In the case of coarse mesh regimes this results in spherical objects being represented as geodetic spheres affecting the fluid flow at the near boundary region. Various algorithms do exist which offer improved tetrahedral/hex meshing for curved surfaces (Alliez, Cohen-Steiner, Yvinec, & Desbrun, 2005; Leland, Melander, Meyers, Mitchell, & Tautages, 1998), however these can only be implemented within CAD-based meshing. The IBM techniques used here generate meshes which are a combination of hexahedral (6-face) and tetrahedral (4-face) cells. The basic cell size is set by the size of the scan voxel which is determined by the MRI resolution; the resulting mesh resolution is therefore the same as the original geometric resolution. Cell size distributions are demonstrated in Fig. 4 and the range of cell volumes detailed in Table 1. There are also complications with the mesh quality in the near

Table 1  
Mesh data.

Property	Value
Max cell vol	$1.54 \times 10^{-9} \text{ m}^3$
Min cell vol	$6.66 \times 10^{-17} \text{ m}^3$
Max face area	$2.51 \times 10^{-6} \text{ m}^2$
Min face area	$1.53 \times 10^{-11} \text{ m}^2$
Overall mesh volume	$1.02 \times 10^{-3} \text{ m}^3$

wall region. The adoption of the SST  $k-\omega$  transitional solver for the turbulent simulations enforces restrictions on the near-wall mesh structure; in particular the laminar sub-layer has to be resolved, resulting in a limit on the size of the cells in the near-wall region. If  $y$  is the distance from the wall of the cell centre of the first row of cells, we define

$$\frac{yu_{\tau}}{\nu} = y^+, \quad \text{where } u_{\tau} = \sqrt{\frac{\tau_0}{\rho}}$$

and the acceptable  $y^+$  values at the wall adjacent cell should be in the region of  $0 < y^+ < 5$ . This is achieved as shown in Fig. 5.

A significant issue with most CFD simulation is the demonstration of mesh independence, in which the calculation is repeated on successively finer meshes until selected parameters are shown to remain invariant under changing mesh density. This is unfortunately not possible for the current calculation. One result of the IBM methodology is the tight linkage between the scan resolution and the resulting mesh. Resampling the data at a different resolution is possible (in fact is one of the tools available with ScanIP) but this changes the geometry as well as the mesh, so successively finer meshes would vary the geometry. The number of cells used here is however comparable with the number used in our previous study using CAD-based meshing techniques Baker and Tabor (2010) for which a mesh sensitivity study was possible; this suggests that the results are robust. Furthermore we are able to estimate the Kolmogorov length scale and compare this to the cell size. The Kolmogorov length scale  $\eta$  can be related on dimensional grounds to the kinematic viscosity  $\nu$  and the dissipation rate  $\varepsilon$  thus:

$$\eta = \left( \frac{\nu^3}{\varepsilon} \right)^{1/4}$$

For the turbulent calculations we are using the  $k-\omega$  model, so  $\varepsilon = \omega k$ . We can use the values from the CFD calculations to estimate the magnitude of  $\eta$ . From the calculations for a mid-range model  $Re_{dp} = 4000$ ,  $k$  in the bed is in the range  $0.5\text{--}1.5 \text{ m}^2 \text{ s}^{-1}$ .  $\omega$  is more

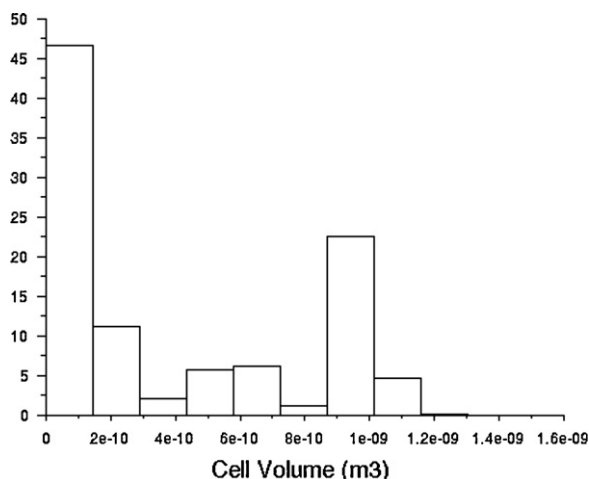


Fig. 4. Mesh element volume distribution.

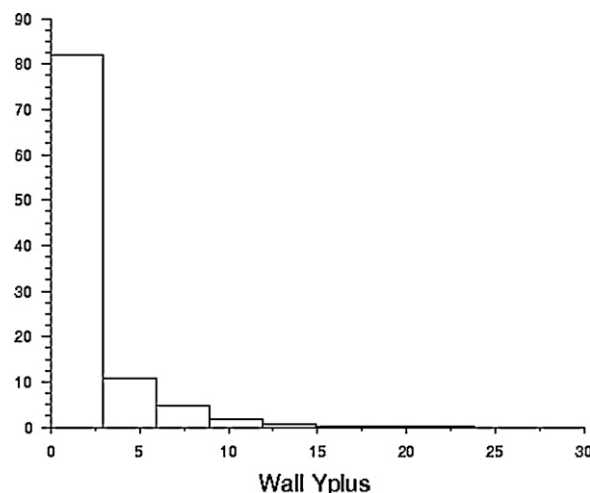


Fig. 5. Mesh  $y^+$  values at near-wall region.

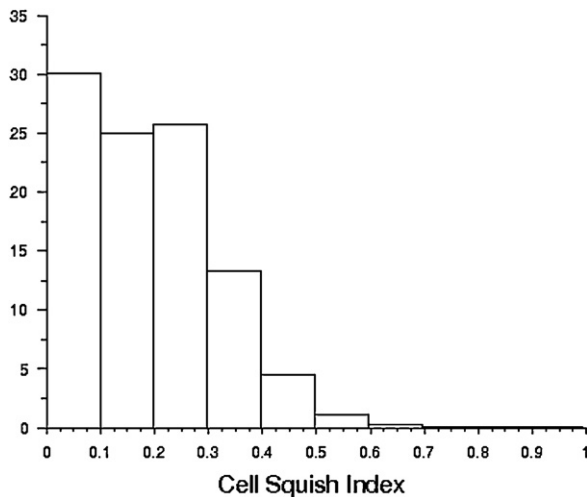


Fig. 6. Mesh cell squish index.

difficult to estimate as it gets very large in the vicinity of the walls, but in the pore spaces within the bed  $\omega \sim 100$ , giving  $\eta \sim 0.1$  mm. The base mesh cell size is based on the scan resolution of 1 mm, but Fig. 4 demonstrates that 46% of the cells have volumes  $< 2 \times 10^{-10}$ , i.e.  $\delta_x < 0.5$ , suggesting that the mesh is nearly able to resolve the smallest turbulent structures in the flow.

In many cases of mesh quality analysis it is desirable to use a non-dimensional parameter, such as cell equivolume skew ( $Eq_{vol}$ ), calculated using the volume deviation method (for tetrahedral meshes) and equiangle skew ( $Eq_{angle}$ ) using the normalised angle deviation method (for mixed tet/polyhedral meshes). For this work we employ the a parameter known as the cell squish index ( $CSk_{index}$ ). The cell squish index uses the dot-products (scalar products) of each vector pointing from the centroid (the node location) of the cell to each of the cell faces and the face area vector associated with each face given as

$$CSk_{index} = \max \left[ 1 - \frac{A_i \cdot r_{c0/xfi}}{|A_i| |r_{c0/xfi}|} \right] \quad (12)$$

where  $A_i$  is the cell face area vectors and  $r_{c0/xfi}$  is the vectors connecting the cell centre to the respective face centre. The closer the  $CSk_{index}$  value is to 1, the more degenerate the cell. Fig. 9a and b presents a contour plot of cell squish index of a random cluster of cylinders within the bed. As expected the plot indicates that the majority of highly skewed elements are located within the vicinity of the interparticulate contact points where two particles meet on a curved surface.

For this work the majority highly skewed elements ( $CSk_{index} > 0.4$ ) are converted to polyhedra using Fluent's built in algorithm. The algorithm evaluates a highly skewed tetrahedral cell and picks an edge and agglomerates the surrounding cells neighbouring the edge and agglomerates the adjoining cells into a polyhedron. We can see from Fig. 6 that the majority of cells fall in the range of  $0 < CSk_{index} < 0.3$  indicating an acceptable mesh quality.

## 6. Results

Fig. 7 demonstrates close agreement between the experimental results (crosses) and the CFD calculations, both with and without the turbulence model switched on. Agreement between the CFD model results with and without turbulence modelling indicates that at these Reynolds numbers and mesh resolution the turbulence model is having next to no effect on the pressure drop. It might be that at much higher Reynolds numbers the two sets of

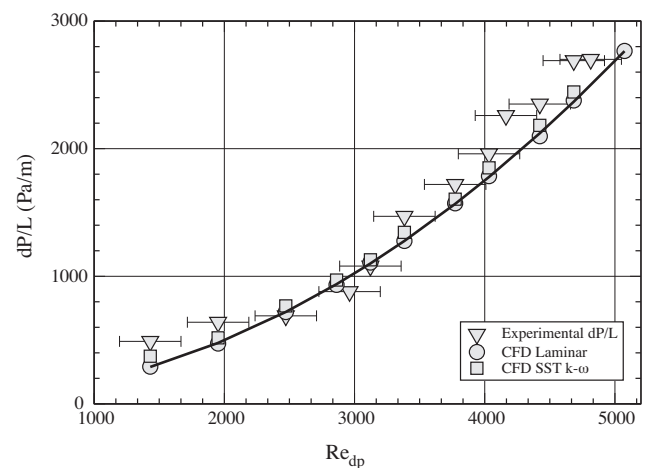


Fig. 7. Pressure drop per unit length as a function of the particle Reynolds number.

results might diverge further, but we have demonstrated above that the mesh resolution for these Reynolds numbers the mesh resolution is approaching the level necessary to explicitly resolve the smallest scale flow structures. The laminar flow calculations might thus be better thought of as representing an under-resolved DNS or implicit LES type of calculation. Fig. 8 compares our experimental and computational results with the empirical correlation of Eisfeld and Schnitzlein (2001), plotting the dimensionless pressure drop  $\phi$  (Eq. (1)). Agreement is close although the empirical correlation slightly overpredicts the dimensionless pressure drop. It should be noted that the correlation of Eisfeld and Schnitzlein (2001) is based on an amalgam of a range of experimental data representing several different geometries, whilst our experiments were performed as far as technically feasible on the exact geometry used for the CFD. With cylindrical packed beds the geometry is significantly more disordered than is the case for spherical particles, in which case pressure drop can vary significantly with each individual pack rendering it difficult to derive a single formula encompassing each individual case. Differences between the CFD with and without turbulence models are minimal, although they are magnified on this plot. In Fig. 7 the main influence on pressure drop is the  $U^2$  term, as seen from its quadratic behaviour with  $Re_{dp}$ . When plotting the dimensionless pressure drop  $\phi$  this factor is removed, leading to the essentially constant  $\phi$  (only changes by a factor of about 3 over the range in Fig. 8) and the magnification of the second order effects such as that of the turbulence model.

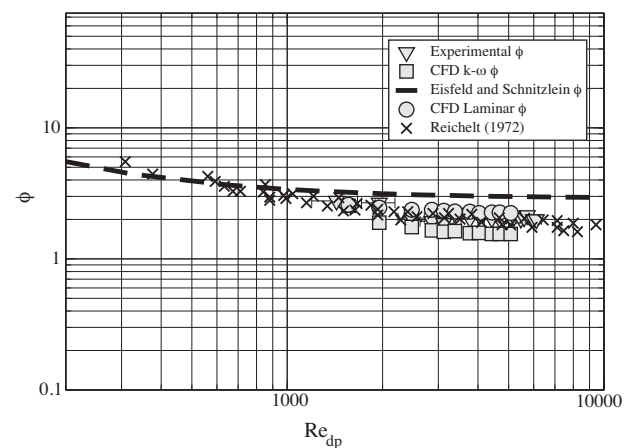
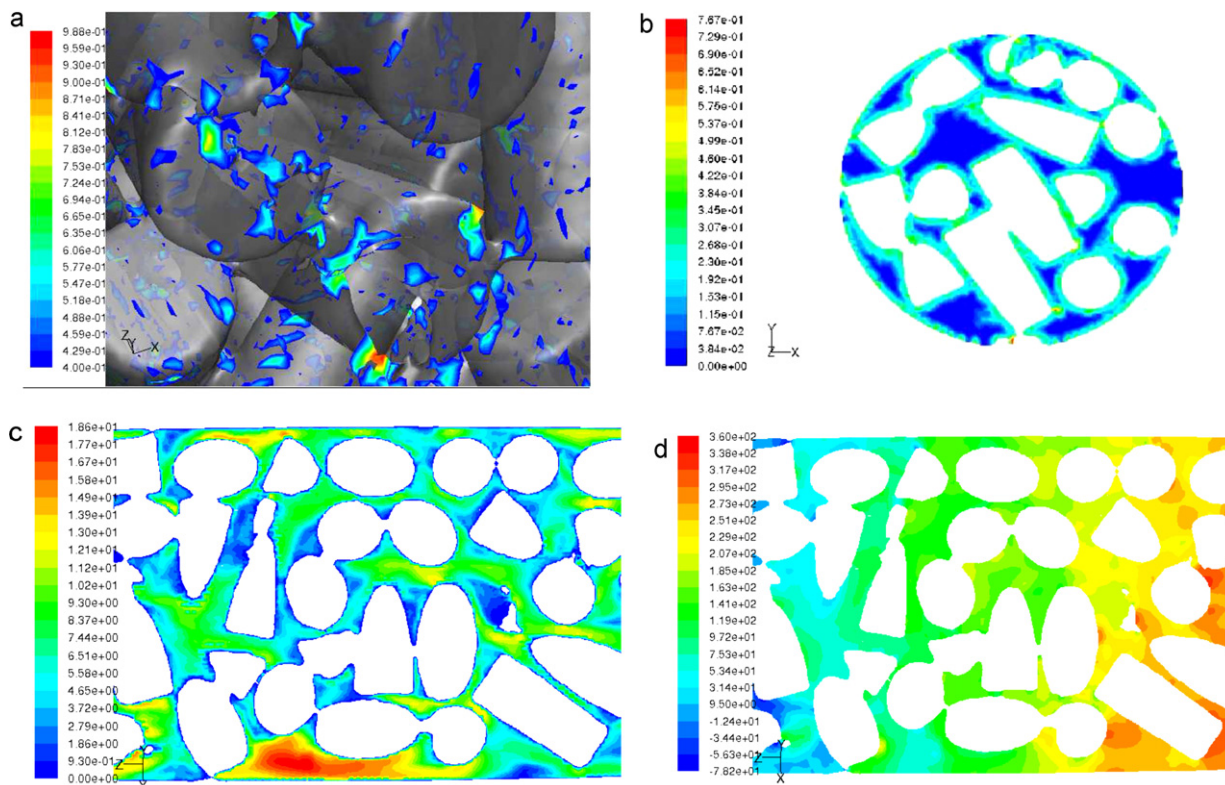


Fig. 8. Dimensionless pressure drop per unit length as a function of the particle Reynolds number.





**Fig. 9.** (a) contours of cell  $CSK_{index} > 0.4$  for a random cluster of cylinders in the geometry; (b) contours of cell squish index for a 2d slice in the x-plane. (c and d) Contours of velocity magnitude and pressure for the cylindrical media plotted on a 2d slice lengthwise through the bed.

One of the main sources of discrepancy between the CFD and experiment can be attributed to the accuracy of reproduction of the geometry through the IBM process, in particular the effect on the mesh of the merging of the media at the interparticulate contact points. With bed particles possessing one or more curved faces, when two or more of these objects touch, the contact point becomes infinitely small. This cannot be resolved by the MRI scan, instead the contact regions are represented by one or more contact voxels leading to a merging of the particles in this region. This is apparent not only visually, but also the discrepancy between experimental porosity and the porosity derived from the computational mesh of  $\delta\epsilon = 0.01$ . Should the scan be carried out with a higher resolution, one would expect a reduction in the interparticle contact region. A related issue is the mesh quality; the distance between surfaces in the region near the contact point results in poor cell quality. This is to some extent ameliorated by the finite resolution of the contact points alluded to earlier; a conventional meshing strategy based on CAD realisations of the particles (which can represent the true curvature of the particles, and thus generates very fine wedges of space to be meshed close to the contact point) creates extreme problems in meshing and generates very poor mesh quality in these regions. When discretised, the size of this contact point is limited to the smallest element which is possible for the meshing software to create. Statistically, due to the geometrically complex domain, the total pressure drop is fairly insensitive to variations in mesh quality, providing the mesh has a suitable quality not to cause simulation divergence. However, when it is desired to analyse flow structure in detail, the mesh is required to be suitably fine to resolve the near wall region.

Although this paper is primarily concerned with the problems associated with the mesh creation of packed beds, the flow heterogeneity is also of interest. Once a computational study has been run, one of the most difficult of problems to solve is post pro-

cessing, in regard to interpreting a suitable visual output and the vast computational effort required due to the number cells. This is further complicated by the issue of trying to view a complex 3d domain in 2 dimensions. This problem is analogous to the problem of the almost impossible use of PIV or LDA techniques when analysing flow through packed beds due not having a direct line of sight through the bed particles. Fluent does offer the option to make the particles translucent, however this only clutters the output and difficult to draw any conclusions. The most realistic approach, and the approach we adopt here, is to cut a 2d plane through the bed in order to interpret the pressure and velocity distribution as a 2d representation, and this is shown in Fig. 9c and d. As expected with low aspect ratio, disordered beds, Fig. 9c shows distinct pathways of mainstream velocity with a good proportion of the flow being channelled in the wall region due to the increased porosity in the region resulting in a higher interstitial velocity.

## 7. Conclusion

Results have shown the accuracy of imaged based meshing as a tool for reconstructing packed beds from geometric information gained from non-invasive methods, such as MRI and CT. It has also shown the ability for imaged based meshing to deal with complex geometries and boundaries, without compromising the final geometry in relation to mesh quality, which traditional meshing software would find virtually impossible. The work has also shown that the finite volume method is a viable alternative to Lattice Boltzmann methods and has shown promising results when compared to experimental data of the exact geometry. The work also suggests that as more computational power becomes available and with the resolution of non-invasive methods increasing, there is much scope for further work on much larger beds of particles.

## References

- Alliez, P., Cohen-Steiner, D., Yvinec, M., & Desbrun, M. (2005). Variational tetrahedral meshing. *ACM Transactions on Graphics*, 24(3), 617–625 (special issue on proceedings of SIGGRAPH).
- Baker, M. J., & Tabor, G. R. (2010). Computational analysis of transitional airflow through packed columns of spheres using the finite volume technique. *Computers and Chemical Engineering*, 34, 878–885.
- Blake, F. C. (1922). The resistance of packing to fluid flow. *Transactions of American Institute of Chemical Engineers*, 14, 415–421.
- Burke, S. P., & Plummer, W. B. (1928). Gas flow through packed columns. *Industrial Engineering Chemistry*, 20, 1196–1200.
- Carman, P. C. (1937). Fluid flow through a granular bed. *Transactions of the Institution of Chemical Engineers (London)*, 15, 150–156.
- Carman, P. C. (1938). *Journal of Society of Chemical Industry*, 57, 225.
- Chaulkin, R., Ahmad, A., Fairweather, M., Jia, X., & Williams, R. (2007). An investigation of sphere packed shell-side columns using a digital packing algorithm. *Computers and Chemical Engineering*, 31, 1715–1724.
- Chaulkin, R., Ahmad, A., Fairweather, M., Jia, X., & Williams, R. A. (2009). Digital predictions of complex cylinder packed columns. *Computers and Chemical Engineering*, 33, 10–21.
- Choi, Y. S., Kim, S. J., & Kim, D. (2008). A semi-empirical correlation for pressure drop in packed beds of spherical particles. *Transport in Porous Media*, 75(2), 133–149.
- Collins, T. P., Tabor, G. R., & Young, P. G. (2007). A computational fluid dynamics study of inspiratory flow in orotracheal geometries. *Medical and Biological Engineering and Computing*, 45(9), 829–836.
- DiFelice, R., & Gibilaro, L. G. (2004). Wall effects for the pressure drop in fixed beds. *Chemical Engineering Science*, 59(14), 3037–3040.
- Eisfeld, B., & Schnitzlein, K. (2001). The influence of confining walls on the pressure drop in packed beds. *Chemical Engineering Science*, 56(14), 4321–4329.
- Ergun, S. (1952). Flow through packed columns. *Chemical Engineering Progress*, 48(2), 89.
- Foumeny, E. A., Benyahia, F., Castro, J. A. A., Moallemi, H. A., & Roshani, S. (1993). Correlations of pressure drop in packed beds taking into account the effect of confining wall. *International Journal of Heat and Mass Transfer*, 36, 536–540.
- Freund, H., Bauer, J., & Zeiser, T. (2005). Detailed simulation of transport processes in fixed beds. *Industrial and Engineering Chemistry Research*, 44(16), 6423–6434.
- Gunjal, P. R., Ranade, V. V., & Chaudhari, R. V. (2005). Computational study of a single-phase flow in packed beds of spheres. *AIChE Journal*, 51, 365–378.
- Issa, R. I. (1986). Solution of the implicitly discretised fluid flow equations by operator-splitting. *Journal of Computational Physics*, 62, 40–65.
- Johnson, E. A. C., & Young, P. G. (2005). On the use of a patient-specific rapid prototyped model to simulate the response of the human head to impact and comparison with analytical and finite element models. *Journal of Biomechanics*, 38(1), 39–46.
- Kozeny, J. (1927). Über Kapillare Leitung des Wassers im Boden, Stizursberichte, Royal Academy of Science, Vienna, proceedings Class I, V. 136, p. 271.
- Leland, R. W., Melander, D. J., Meyers, R. W., Mitchell, S. A., & Tautages, T. J. (1998). The geode algorithm: Combining hex/tet plastering, dicing and transition elements for automatic, all-hex mesh generation. In *Seventh international meshing roundtable* Dearborn, Michigan, (pp. 515–521).
- Logtenberg, S. A., & Dixon, A. G. (1998). Computational fluid dynamics of fixed bed heat transfer. *Chemical Engineering Process*, 37, 7–21.
- Mantle, M. D., Sederman, A. J., & Gladden, L. F. (2001). Single and two-phase flow in fixed bed reactors: MRI flow visualisation and lattice-boltzmann simulations. *Chemical Engineering Science*, 56, 523–529.
- Manz, B., Warren, P. B., & Gladden, L. F. (1999). Flow and dispersion in porous media: Lattice Boltzmann and NMR studies. *AIChE Journal*, 45, 1845–1854.
- Menter, F. (1994). Two-equation eddy-viscosity turbulence models for engineering applications. *AIAA Journal*, 32(8), 1598–1605.
- Montillet, A., & Coq, L. L. (2001). Characteristics of fixed beds packed with anisotropic particles – Use of image analysis. *Powder Technology*, 121, 138–148.
- Nguyen, N. L., van Buren, V., Reimert, R., & von Garnier, A. (2005). Determination of porosity and flow distribution in packed beds by magnetic resonance imaging. *Magnetic Resonance Imaging*, 23, 395–396.
- Patankar, S. V., & Spalding, D. B. (1972). A calculation procedure for heat, mass and momentum transfer in 3-d parabolic flow. *International Journal of Heat and Mass Transfer*, 15, 1787.
- Perry, R. H., & Green, D. W. (1997). *Perry's chemical engineers handbook* (7th edition). New York: McGraw-Hill.
- Puyou, M., Charriere, E., Streicher, R., & Young, P. G. (2004). Post clinical assessment of implant performance: Finite element models of an implanted femur and hip based on in vivo CT scan data. In *6th international symposium on computer methods in biomechanics and biomedical engineering* Madrid.
- Reichelt, W. (1972). Zur berechnung des druckverlustes einphasig durchstromter kugel- und zylinderschuttungen. *Chemie-Ingenieur-Technik*, 44, 1068–1071.
- Ren, X., Stapf, S., & Blumich, B. (2005). NMR velocimetry of flow in model fixed-bed reactors of low aspect ratio. *AIChE Journal*, 51(2), 392–405.
- Sharma, S., Mantle, M. D., Gladden, L. F., & Winterbottom, J. M. (2001). Determination of bed voidage using water substitution and 3d magnetic resonance imaging, bed density and pressure drop in packed bed reactors. *Chemical Engineering Science*, 56, 587–595.
- Tabor, G., Yeo, O., Young, P. G., & Laity, P. (2008). CFD simulation of flow through an open-cell foam. *International Journal of Modern Physics C*, 19(5), 703–715.
- Tabor, G., Young, P. G., Beresford-West, T., & Benattayallah, A. (2007). Mesh construction from medical imaging for multiphysics simulation: Heat transfer and fluid flow in complex geometries. *Engineering Applications of Computational Fluid Mechanics*, 2(1), 126–135.
- Tóbis, J. (2000). Influence of bed geometry on its frictional resistance under turbulent flow conditions. *Chemical Engineering Science*, 55, 5359–5366.
- Versteeg, H. K., & Malalasekera, W. (1995). An introduction to computational fluid dynamics: The finite volume method. *Longman Scientific & Technical*.
- Wang, Z., Afacan, A., Nandakumar, K., & Chuang, K. T. (2001). Porosity distribution in random packed columns by gamma ray tomography. *Chemical Engineering and Processing*, 40, 209–219.
- Young, P. G., Beresford-West, T. B. H., Coward, S. R. L., Notarberardino, B., Walker, B., & Abdul-Aziz, A. (2008). An efficient approach to converting 3d image data into highly accurate computational models. *Philosophical Transactions of the Royal Society of London A*, 366, 3155–3173.
- Zhang, W., Thompson, K. E., Reed, A. H., & Beenken, L. (2006). Relationship between packing structure and porosity in fixed beds of equilateral cylindrical particles. *Chemical Engineering Science*, 61, 8060–8074.
- Ziolkowska, I., & Ziolkowska, D. (1988). Fluid flow inside packed beds. *Chemical Engineering and Processing*, 23, 137–164.
- Zunarelli, L., & Young, P. G. (1999). *Analytical and numerical modelling of head injury mechanisms. Simulation and modelling techniques applied to medicine*. London: Institute of Physics.